Experimental results: The devices were characterised using an end-fire coupling set-up in which light is launched into the waveguide using a microscope objective (×40, 0·6 NA) focused on the entrance facet of the sample. Input light is TE polarised. In the case of devices without integrated detectors, light intensity in both output arms was measured using another microscope objective (×100) which imaged the near field pattern either onto an IR video camera or onto a Ge detector. For switches with detectors, we only measured the photocurrent in each detector (which actually appears to be easier). The light source was a Fabry–Perot InP/GaInAsP laser at $\lambda = 1{\cdot}52\,\mu m$. Electrical measurements were performed using probe needles brought in contact with the bonding pads.

Fig. 3 shows the reverse I/V curve of one detector, with and without incoming light. It can be seen that reverse dark currents are very low (below 1 nA at −5 V). Photocurrents are found to remain constant over the whole bias range, indicating low residual dopings with a detecting region fully depleted at 0 V. The capacitance of the detectors is of the order of 1 pF. This rather high capacitance is because of the fact that, on a

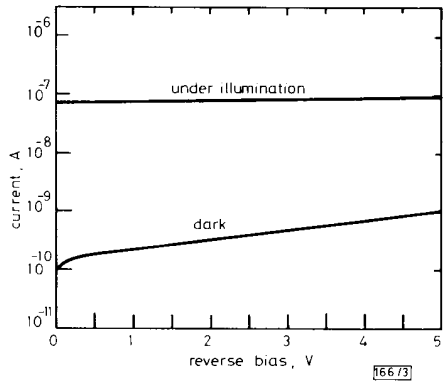

Fig. 3 *I/V curves on an integrated photodiode*

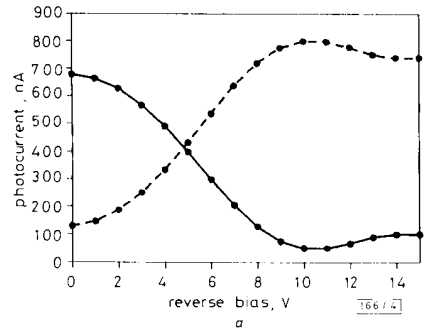

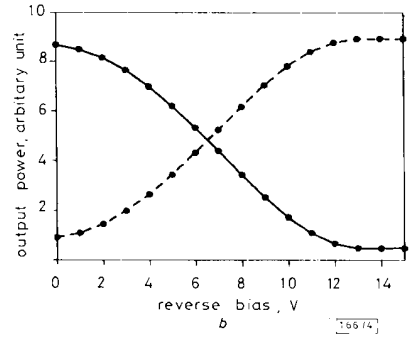

Fig. 4 *Switching curves of directional couplers*
a Integrated photodetectors; length = 3 mm
b External photodetectors; length = 2 mm

n-doped substrate, bonding pads contribute to the global capacity. We have shown that, for the same process on semi-insulating substrate, very low capacitances could be obtained.[1] This parameter could also be lowered by increasing the thickness of the dielectric layer under the bonding pads.

Switching curves were recorded either with external detectors as described above or with integrated ones. The results in both cases, recorded for different switches on the same chip, are shown in Fig. 4. The switching voltage is rather high, (~14 V) compared with our previous results.[4,5] This is because of a non-optimal etched depth. Indeed the etched depth was a little too low, which decreased the coupling lengths of the devices. The refractive index change necessary for switching a directional coupler is inversely proportional to its coupling length and not to its actual length.[6] Phase modulation efficiency, can be deduced from the experimental switching curves. It is of the same order of magnitude (12°/V/mm) as in our previous work.

Conclusion: These results demonstrate for the first time the successful integration of an optical switch based on InP with detectors. The process used was not found to diminish performances of devices previously demonstrated separately.

Acknowledgments: This work has been partly supported by the EEC through the RACE project OSCAR (R1033).

J. A. CAVAILLÈS
M. RENAUD
P. JARRY
M. ERMAN
J. F. VINCHANT
A. GOUTELLE

Laboratoires d'Electronique Philips (LEP)
22, Avenue Descartes, 94453 Limeil-Brévannes, France

10th September 1990

References

1 ERMAN, M., RIGLET, P., JARRY, P., MARTIN, B. G., RENAUD, M., VINCHANT, J.-F., and CAVAILLES, J. A.: 'Optical circuits and integrated detectors', to be published in *IEE Proc. J, Special Issue on Semiconductors Optoelectronics*

2 RIGLET, P., ERMAN, M., MARTIN, B. G., JARRY, P., and RENAUD, M.: 'High performance PIN photodiodes on waveguide for coherent communications'. Proc. ECOC'90, Amsterdam, 16th–20th September 1990, TuG4.2

3 LIOU, K.-Y., KOREN, U., CHANDRASEKHAR, S., KOCH, T. L., SHAHAR, A., BURRUS, C. A., and GNALL, R. P.: 'Monolithic integrated InGaAsP/InP distributed feedback laser with Y branching waveguide and a monitoring photodetector grown by metalorganic chemical vapour deposition', *Appl. Phys. Lett.*, 1989, (2), pp. 114–116

4 ANGENENT, J. H., ERMAN, M., THIJS, P. J. A., RENAUD, M., GRAVER, C., AUGER, J. M., GAMONAL, R., and CAVAILLES, J. A.: 'Optical switches on InP substrates using carrier depletion with driving voltages as low as 4·5 Volts'. Proc. ECOC'89, Gothenburg, 10th–14th September 1989

5 CAVAILLES, J. A., ERMAN, M., JARRY, P., AUGER, J.-M., GOUTELLE, A., and ANGENENT, J. H.: 'Cascaded carrier depletion optical switches based on InP/GaInAsP waveguides'. Proc. ECOC'90, Amsterdam, 16th–20th September 1990, TuB2.2

CALCULATED CHIRP IN INTRACAVITY LOSS MODULATED DFB LASERS

Indexing terms: Semiconductor lasers, Linewidth

Calculations of modulation induced line-width broadening in 1·55 μm DFB lasers are reported. Voltage controlled intracavity loss modulation has significant performance advantages compared with conventional large signal current modulation schemes.

Dynamic spectral broadening, or chirp, is of considerable importance for long distance, high bit rate optical communications at 1·55 μm. The limits placed on high bit rate communications by wavelength chirp of single mode DFB laser

sources has recently been investigated.[1,2] Henmi *et al.*,[1] have shown that when a laser is modulated from a bias point below (or close to) threshold, significant amounts of optical power feed into the short wavelength side of the main mode placing a serious limitation on long haul, high bit rate fibre transmission systems. Their experimental results are successfully explained by consideration of single mode laser carrier dynamics. We calculate spectra of DFB lasers under both conventional current modulation and with voltage controlled intracavity loss modulation (ICLM).[3] Contrary to simplistic expectations, voltage controlled ICLMs exhibit superior performance at high bit rates compared with conventional current modulation schemes.

The single mode rate equations may be written as

$$\frac{dn}{dt} = \frac{I_G}{ev} - R \tag{1}$$

$$\frac{dp}{dt} = \left[\Gamma G - \frac{1}{\tau_p'}\right]p + R_{sp} \tag{2}$$

where p is the photon density, n is the carrier density, R is the charge carrier recombination rate, G is the gain function, R_{sp} is the spontaneous emision coupling into the lasing mode, v is the active region volume, Γ is the confinement factor, $1/\tau_p'$ describes the total losses in the laser and I_G is the gain section current which is held constant in ICLM. We may model an ICLM laser by writing[4]

$$\frac{1}{\tau_p'} = \frac{1}{\tau_p}[1 + r_1 + r_2 V_S + r_3/(1 + I/I_S)] \tag{3}$$

where $(1/\tau_p)[= (c/\mu)(\alpha_0 + \alpha_m)]$ describes the familiar internal, α_0, and mirror, α_m, losses. V_S is the voltage applied to the absorbing segment, $I_S = I_{S0}(1 + \kappa V_S)$ is the absorption saturation intensity which increases with increasing reverse bias and r_1, r_2 and r_3 are parameters describing the dependence of saturable and nonsaturable absorption on voltage for lasers of different geometries. When the terms describing the absorption modulation (r_1, r_2, r_3, V_S, and I_S) are set to zero and I_G is varied, eqns. 1–3 revert to the conventional form for a current modulated laser.

The recombination rate, R, is expressed explicitly in terms of the carrier density

$$R = (A_{nr} + Bn + Cn^2)n + Gp \tag{4}$$

where A_{nr}, B and C describe nonradiative and radiative recombination processes in the semiconductor.[5] We assume that the laser gain is a linear function of carrier density but is subject to gain saturation,[6] i.e., $G = A(n - n_0)(1 - \varepsilon p)$ where n_0 is the carrier density required for transparency, A is the gain constant and ε ($\ll 1{\cdot}0$) is a gain saturation parameter. Spontaneous emission coupling into the lasing mode is given by $R_{sp} = \beta\Gamma Bn^2$. The linear dependence of refractive index, μ, on the carrier density and confinement factor,[7] i.e., $d\mu/dn = -\Gamma\rho$, where ρ is a constant of proportionality, leads to a carrier density induced change in wavelength

$$\Delta\lambda = -\frac{\Gamma\rho\lambda}{\mu}\Delta n \tag{5}$$

Eqns. 1–4 are integrated with a fourth order Runge–Kutta integrator using parameter values given in Table 1. Eqn. 5 is then used to calculate the refractive index and wavelength change with time. The maximum and minimum of the wavelength spectrum is divided into 500 intervals and the optical power within each wavelength interval is determined. A Gaussian instrumental broadening function of waist $\approx 0{\cdot}007$ nm is then passed over the array. To provide meaningful comparison between the different modulation schemes, currents and voltages are set such that 2 mW of optical power is switched in each case.

Figs. 1–3 show the emitted optical power, carrier density variation and calculated spectral broadening for three laser modulation schemes; (Fig. 1) digital (on–off) voltage controlled ICLM, (Fig. 2) current modulation from below to above threshold (on–off) and (Fig. 3) current modulation where the total applied current remains above threshold (on–on). In all cases the devices are modulated from $t = 0$ ns with a 1 Gbit/s 1010 ... data stream. The calculated light output in

Table 1 MODELLING PARAMETERS

Parameter	Value
A	10^{-6} cm^3 s^{-1}
n_0	10^{18} cm^{-3}
A_{nr}	10^8 s^{-1}
B	10^{-10} cm^3 s^{-1}
C	8×10^{-29} cm^6 s^{-1}
τ_p	$1{\cdot}84 \times 10^{-12}$ s
v	$3{\cdot}6 \times 10^{-11}$ cm^3
μ	4
β	2×10^{-5}
λ	$1{\cdot}5\,\mu$m
ε	4×10^{-17} cm^3
Γ	0·2
r_1	0·15
r_2	$-0{\cdot}26$ V^{-1}
r_3	3
I_s	30 kW cm^{-2}
κ	$-1{\cdot}2$ V^{-1}
ρ	$4{\cdot}5 \times 10^{-21}$ cm^3

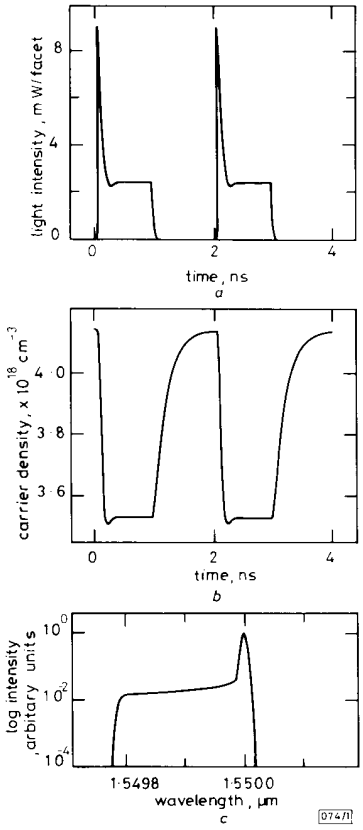

Fig. 1 *Calculated switching characteristics*
2 mW optical power per facet by application of $0 < V_S < 1$ V 1010 ... 1 Gbit/s data stream to intracavity loss modulated DFB
$I_G = 45$ mA
a Optical power output
b Carrier density variation
c Time averaged optical spectra

each case shows relaxation oscillations accompanying the switching transient, ICLM showing the greatest relaxation oscillation spike because of the large stored carrier number in the off state. With conventional on–on modulation, relaxation oscillations are seen at both the 1 and the 0 state. Comparing Figs. 1*a* and 2*a* a greater turn-on delay is associated with conventional off–on modulation than with ICLM. This results from a smaller carrier density in the off state of the conventional scheme and a recombination time dependence on carrier density. Of particular importance are the magnitude and duration of the relaxation oscillation replicas in the carrier densities and the carrier density recovery times.

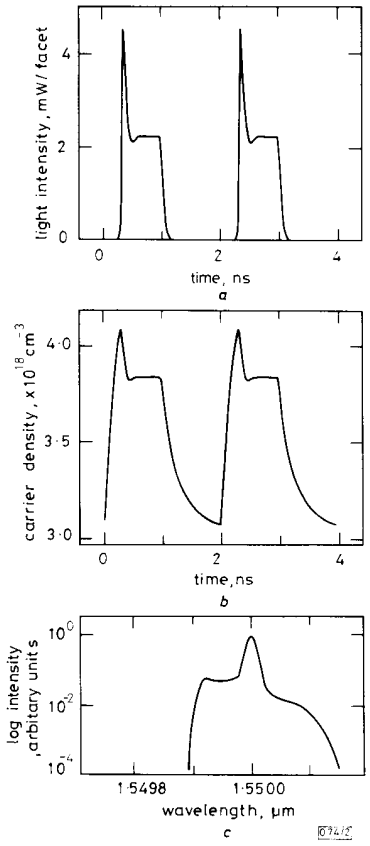

Fig. 2 *Calculated switching characteristics*
2 mW optical power per facet by application of 33 mA current pulses riding on a 20 mA DC bias current
Laser threshold is 35 mA
a Optical output power
b Carrier density variation
c Time averaged optical spectra

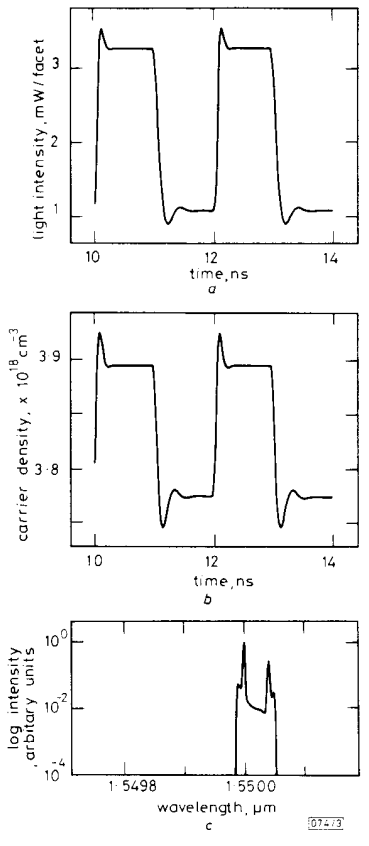

Fig. 3 *Calculated switching characteristics*
2 mW optical power per facet by application of 19 mA current pulses with a laser DC bias current of 43 mA
Laser threshold is 35 mA
a Optical output power
b Carrier density variation
c Time averaged optical spectrum

It is apparent from Figs. 1–3 that the spectral shift caused by the carrier density variations is of increasing importance as the bit duration approaches that of the relaxation oscillation spike. For the current modulated on–off scheme (Fig. 2*c*), in addition to a broadening of the main mode (full width at half maximum (FWHM) of 0·02 nm) we find that a pronounced shoulder is generated on the short wavelength side of the main mode. Lesser broadening of the main mode (Fig. 1*c*) is predicted for ICLM (FWHM of 0·01 nm), arising from the rapid carrier dynamics associated with the Q-switched process. The brevity of the relaxation oscillation transient and the larger carrier number excursion accompanying it also means that the spectral power in the short wavelength shoulder extends over a greater wavelength interval, leading to an enhanced shoulder/main mode intensity ratio. With the conventional on–on case (Fig. 3*c*), two comparable spectral peaks separated by 0·04 nm are predicted corresponding to the mark and space of the modulation cycle. Each of these peaks have associated spectral shoulders caused by relaxation oscillation in carrier density.

These results have considerable implications for high bit rate lightwave communications which generally make use of digital (on–off) modulation. Naively, one might expect the large carrier density excursions accompanying ICLM to induce prohibitive spectral broadening for long distance transmission systems. Our calculations show that the large carrier density variation and giant relaxation oscillation spike co-operate to produce a narrower spectrum and greater spectral contrast than in conventional current modulated digital schemes without external optical elements.[8] In the conventional above threshold scheme (on–on) the spectral peak corresponding to the 0 state also produces, from a transmission viewpoint, a substantial effective spectral width. It is apparent, from the calculated carrier density variations, that a spectral pattern effect caused by incomplete carrier recovery will place constraints on bit rates and data formats in any digital on–off modulation scheme.

J. O'GORMAN
A. F. J. LEVI
AT&T Bell Laboratories
Murray Hill, New Jersey 07974, USA

31st August 1990

References

1 HENMI, N., FUJITA, S., YAMAGUCHI, M., SHIKADA, M., and MITO, I.: 'Consideration on influence of directly modulated DFB LD spectral spread and fiber dispersion in multigigabit-per-second long-span optical-fiber transmission systems', *IEEE J. Lightwave Technol.*, 1990, **LT-8**, pp. 936–944

2 CORVINI, P. J., and KOCH, T. L.: 'Computer simulation of high-bit-rate optical fiber transmission using single-frequency lasers', *IEEE J. Lightwave Technol.*, 1987, **LT-5**, pp. 1591–1595

3 SUNDARESAN, H., and WICKENS, G. E.: 'Very high amplitude, minimal chirp optical pulse generation at 1·55 μm using multi-contact DFB's and an erbium doped fibre amplifier', *Electron. Lett.*, 1990, **26**, pp. 725–727

4 LEVI, A. F. J., NOTTENBURG, R. N., NORDIN, R. A., TANBUN-EK, T., and LOGAN, R. A.: 'Multielectrode quantum well laser for digital switching', *Appl. Phys. Lett.*, 1990, **56**, pp. 1095–1097

5 O'GORMAN, J., LEVI, A. F. J., NOTTENBURG, R. A., TANBUN-EK, T., and LOGAN, R. A.: 'Dynamic and static response of multielectrode lasers', to be published in Applied Physics Letters

6 AGRAWAL, G. P., and DUTTA, N. K.: 'Long wavelength semiconductor lasers' (Van Nostrand Reinhold, New York, 1986)

7 CHANNIN, D. C.: 'Effect of gain saturation on injection laser switching', *J. Appl. Phys.*, 1979, **50**, pp. 3858–3860

8 MANNING, J., OLSHANSKY, R., and SU, C. B.: 'The carrier induced index change in AlGaAs and 1·3 μm InGaAsP diode lasers', *IEEE J. Quantum Electron.*, 1983, **QE-19**, pp. 1525–1530

VELOCITY FIELD COMPUTATION USING NEURAL NETWORKS

Indexing term: Neural networks

A new approach for optical flow (image velocity) fields computation is presented using computational neural networks. The computational procedure consists of three stages: estimation of the parameters of the neural network model, dynamic measurement of the perpendicular velocity components of the contours or region boundaries and computation of the image velocity fields. The parameters are estimated by comparing the energy function of the neural network with a constrained error function. The nonlinear velocity fields computation method is then carried out iteratively by using a dynamic algorithm to minimise the energy function simultaneously with the dynamic measurement of the perpendicular velocity components by a dynamic procedure. Experiments generate velocity fields that are meaningful and consistent with visual perception.

Introduction: A popular approach to motion analysis of an image sequence is optical flow or image velocity fields computation and interpretation. Computed optical flow fields are an estimation of local velocities subject to certain constraints. In most studies, local variations of grey-level values in consecutive images are used to estimate local velocities. The grey value variations do not provide sufficient information for direct computation of the velocity field except at a corner or other uniquely identifiable image point.[1,2]

It is also possible to compute the optical flow field from moving contours or region boundaries. The motion and shape changes of contours or region boundaries in an image sequence can often be described by functions or transformations. In particular, linear and quadratic transformations are commonly used for 2D and 3D motion analysis and image velocity fields can be generated indirectly from the transformations.

A method has been developed to dynamically estimate image velocity fields that satisfy certain functional forms.[3] The linear and nonlinear transformations are regarded as objective functions. These functions can serve as semi-global smoothness constraints in place of conventional local smoothness constraints.

Neural networks model containing redundant neurons was used to compute image velocity fields.[3] The neural network used here is not a conventional nonlinear discrete network but a nonlinear continuous one. The velocity vector of each point on the contour or region boundary is composed of two components, one is the x-oriented component and the other is the y-oriented component. The velocity component values are represented by the simple sum of the neuron state variables which can take any value between 0 and 1. We call this kind of neural network a continuous neural network not a discrete neural network.[4,6]

In the first stage, the parameters of the neural network are estimated by comparing the energy function of the neural network with the constrained error function. The nonlinear image velocity field computation algorithm is then implemented using a dynamic iterative algorithm to minimise the energy function of the neural network. Meanwhile the velocity component in the normal direction of each point on the contour or region boundary is measured by a dynamic procedure.

The interconnection strengths (also called weights) of the neural network for velocity field computation are known from some parameters. The neurons input biases are also known from some parameters as are the tentative velocity components values. The whole structure of the neural network used here is composed of some identical networks. The number of these networks equals the number of points on the contour or region boundary.

Linear objective function: Let $X^T = (x, y)$ be an image point and

$$U^T = U^T(X) = [u(x, y), v(x, y)] \tag{1}$$

be the velocity vector, where the superscript T denotes transpose. The image point X is moved to X' in one unit time, and hence

$$U = X' - X \tag{2}$$

Consider an affine or linear transformation

$$\hat{U} = AX + C \tag{3}$$

where A is a 2×2 matrix and C is a vector. After segmentation the motion of an contour or boundary is measured by a local motion detector. The local motion detector extracts the component in the direction perpendicular to the local orientation of the boundary. Let $\boldsymbol{n}$ be the unit normal vector, and $v^\perp$ be the component of U in the normal direction. Clearly

$$v^\perp = U^T\boldsymbol{n} \tag{4}$$

Consider N points on a boundary of a region with velocity vectors $U_i^T = (u_i, v_i)$, $i = 1, 2, \ldots, N$. From eqns. 2 and 4, one wishes to minimise

$$\varepsilon = \varepsilon_1 + \beta\varepsilon_2 = \sum_{i=1}^{N} (U_i^T\boldsymbol{n}_i - v_i^\perp)^2 + \beta \sum_{i=1}^{N} |U_i - \hat{U}_i|^2 \tag{5}$$

where β is a weighting factor or regularisation parameter that expresses the confidence in the linear objective function.

Dynamic estimation algorithms: The aperture problem is a major theoretical difficulty as noted by Hildreth.[7] The moving boundaries in consecutive frames allow measurement of a perpendicular velocity component, $v_i^\perp$, for the image point X_i. If there is a significant tangential component in the true velocity $U_i = U(X_i)$, its perpendicular component is not exactly equal to $v_i^\perp$, as shown in Fig. 1. Strictly speaking, the velocity field computed from measurements in the direction perpendicular to the boundaries or contours will not be correct.

If the velocity field is computed by a relaxation algorithm, it is possible to measure at the mth iteration, $v_i^\perp(m)$, and use it to replace $v_i^\perp$. The procedure for dynamic estimation of $v_i^\perp(m)$ is illustrated in Fig. 1. A measured perpendicular component is then defined

$$v_i^\perp(m) = \boldsymbol{n}_i^T U_i'(m) \tag{6}$$